Supplementary Information

Chemicals and materials

Seaweed was obtained from northwestern Pacific shores. Niobium pentachloride ($NbCl_5$, Aladdin, 99.9%), sodium alginate (CP grade, Sinopharm), hydrochloric acid (HCl, 36%-38%), absolute ethanol (C_2H_5OH, ≥ 99.7%), potassium hydroxide (KOH, ≥ 85%) were purchased from Sinopharm Chemical Reagent Co., Ltd. The purity of N_2 is 99.99%. Deionized water was used throughout the whole experiment. All chemicals were used as received without further purification.

Materials synthesis

T-Nb_2O_5/C hybrid: First, $NbCl_5$ was dissolved in deionized water (DI water) to obtain a 5 wt% $NbCl_5$ aqueous solution. Then appropriate amount of HCl solution was added to the above-mentioned solution to slow down the hydrolysis of $NbCl_5$. Then, a 1.5 wt% sodium alginate (SA) aqueous solution was dripped into the $NbCl_5$ solution (volume ratio = 2: 5) under magnetic stirring for 24 h to form Nb-alginate hydrogel beads. After washing with DI water and freeze-drying for 72 h, the Nb-alginate aerogel beads were carbonized at 700 °C for 2 h under N_2 atmosphere. Finally, the obtained black powders were washed with DI water and ethanol for several times, and dried at 60 °C to obtain the T-Nb_2O_5/C hybrid.

T-SDC: First, dried seaweed was carbonized at 600 °C for 3 h under N_2 atmosphere. Then the obtained charcoals were washed with 5 M HCl for 12 h and rinsed with DI water until pH=7. Next, the charcoals were mixed with KOH aqueous solution with a weight ratio of 1:4 (charcoals: KOH). After drying in air, the mixture was heated at 750 °C for 1 h under N_2 atmosphere. The obtained sample was washed thoroughly with 5 M HCl for 2 h and rinsed with DI water until pH=7. Finally, the sample was carbonized at 800 °C for 1 h under N_2 atmosphere to obtain the T-SDC.

Characterizations

X-ray diffraction (XRD) patterns were obtained with a Rigaku Ultima IV Powder Diffractometer (Cu Kα radiation, $\lambda = 0.15406$ nm, sweeping speed: 5° min^{-1}). Scanning electron microscopy (SEM) images were taken using a Mira 3 LHM SEM microscope (5 kV, Tescan, Czech). Transmission electron microscopy (TEM), high resolution transmission electron microscopy (HRTEM) and selected area electron diffraction (SAED) images were taken on a FEI TALOS F200X field-emission TEM microscope (200 kV, America). Raman spectra were recorded on a Renishaw inVia reflex spectrometer using laser excitation of 532 nm. XPS spectra were used to analyze the valence states of Nb and other elements with a Kratos Axis Ultra^{DLD} spectrometer. All XPS spectra were calibrated according to the C 1s peak (284.8 eV) of adventitious carbon on the sample surface. Nitrogen sorption isotherms were measured with a Micromeritics ASAP 2020 adsorption analyzer at 77.4 K and the pore size distributions were calculated by a quenched solid DFT method, assuming a slit pore model for nitrogen adsorption data. Thermogravimetric analysis (TGA) was conducted on a PerkinElmer Pyris 1 TGA instrument with a heating rate of 10 °C min^{-1} under air.

Electrochemical measurements

The electrochemical performances were measured on a multi-channel electrochemical workstation (Biologic VMP3). In the electrode preparation process, it is usually necessary to add conductive agents (such as super-P) and binders (such as PVDF and SA). The conductive agent can reduce the contact resistance of the electrode, accelerate the electron transport rate and improve the ion migration rate in the electrode material, efficiently increasing the charge-discharge rate of the electrode. The binder mainly has the function of binding and preserving the active material, so that the material is not easy to fall off from the current collector. The active materials of T-Nb_2O_5/C hybrid and T-SDC were respectively mixed with super-P and SA at a weight ratio of 8: 1: 1. Control samples of T-Nb_2O_5/C-PVDF (dissolved in N-methyl-2-pyrrolidone, NMP), T-SDC-PVDF, AC-PVDF and AC-SA were prepared in a similar way. Then the slurry was uniformly coated onto Cu foil (for T-Nb_2O_5/C) / Al foil (for T-SDC and AC) and dried at 110 °C for 12 h. Subsequently, the prepared electrodes were pressed at 4 MPa for 1 min and dried at 110 °C for another 12 h in vacuum. The mass loading of anode active materials is 0.8-1.2 mg cm^{-2}. Standard CR2016-type coin cells were assembled using the as-prepared electrodes as cathodes and lithium foil as anodes in an Ar atmosphere. The electrolyte was composed of $LiPF_6$ (1 M) in ethylene carbonate/dimethyl carbonate/ethyl methyl carbonate (volumetric ratio = 1: 1: 1). The cyclic voltammetry (CV) curves were obtained at a scan rate of 0.2 mV s^{-1} in a voltage window of 1.0-3.0 V (for T-Nb_2O_5/C) / 2.0-4.5 V (for T-SDC and AC) (*vs.* Li/Li^+). The electrochemical impedance spectroscopy (EIS) spectra were measured over a frequency range from 1 MHz to 100 mHz with a sinusoidal voltage of 10 mV at open circuit potential (~ 2.7 V for T-Nb_2O_5/C, ~ 3.5 V for T-SDC and AC) (*vs.* Li/Li^+). The discharge-charge process was conducted in a potential window of 1.0-3.0 V (for T-Nb_2O_5/C) / 2.0-4.5 V (for T-SDC and AC) (*vs.* Li/Li^+).

LICs were assembled using the pre-activated T-Nb_2O_5/C anodes and T-SDC or AC cathodes with a weight ratio of 1:3 (anodes: cathodes) in CR2016-type coin cells, and the electrolyte was the same as above. The specific energy and average power densities were calculated by numerically integrating the galvanostatic discharge curves using the two equations: $E=\int_{t1}^{t2} IV\,\mathrm{d}t$ and $P=E/t$, where I is the constant current density (A g^{-1}), V is the voltage (V), $t1$ and $t2$ are the start/end-of-discharge time (s) of LICs, and t is the discharge time (s).

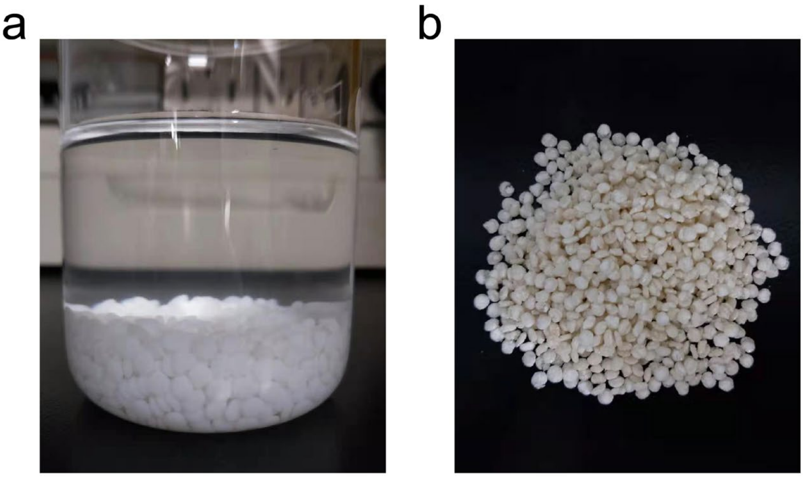

Fig. S1 Digital photographs of (a) self-crosslinking Nb/SA gels and (b) freeze-dried globules.

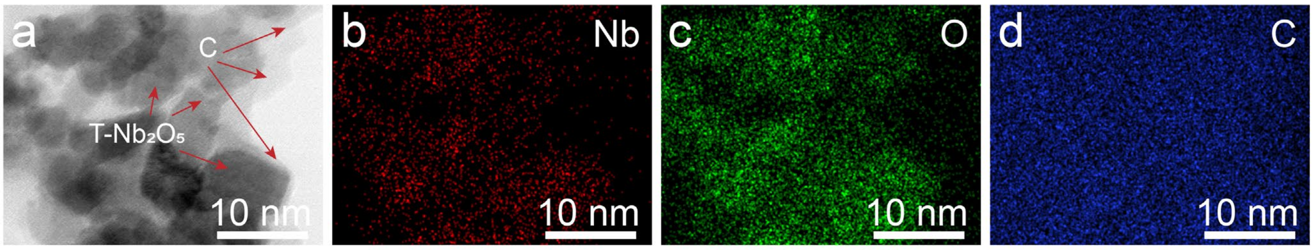

Fig. S2 (a) TEM image and (b-d) the corresponding elemental maps at high magnification of T-Nb_2O_5/C hybrid.

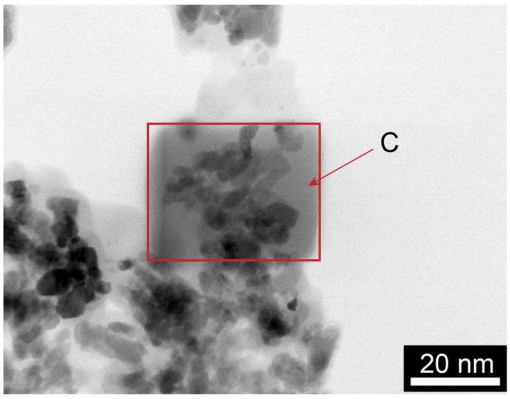

Fig. S3 TEM image after elemental analysis of T-Nb_2O_5/C hybrid.

Due to the accumulation of carbon during the elemental analysis process and the interference of C elements in the air (the red rectangle in Fig. S3), the edges of the carbon layers cannot be clearly observed (Fig. S2d).

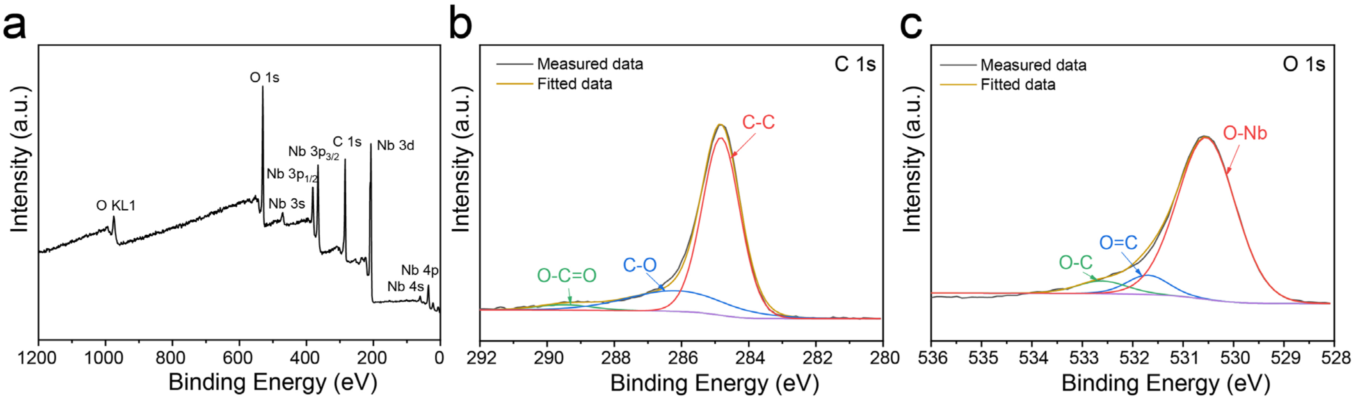

Fig. S4 XPS spectra of T-Nb_2O_5/C hybrid: (a) full, (b) C 1s, (c) O 1s.

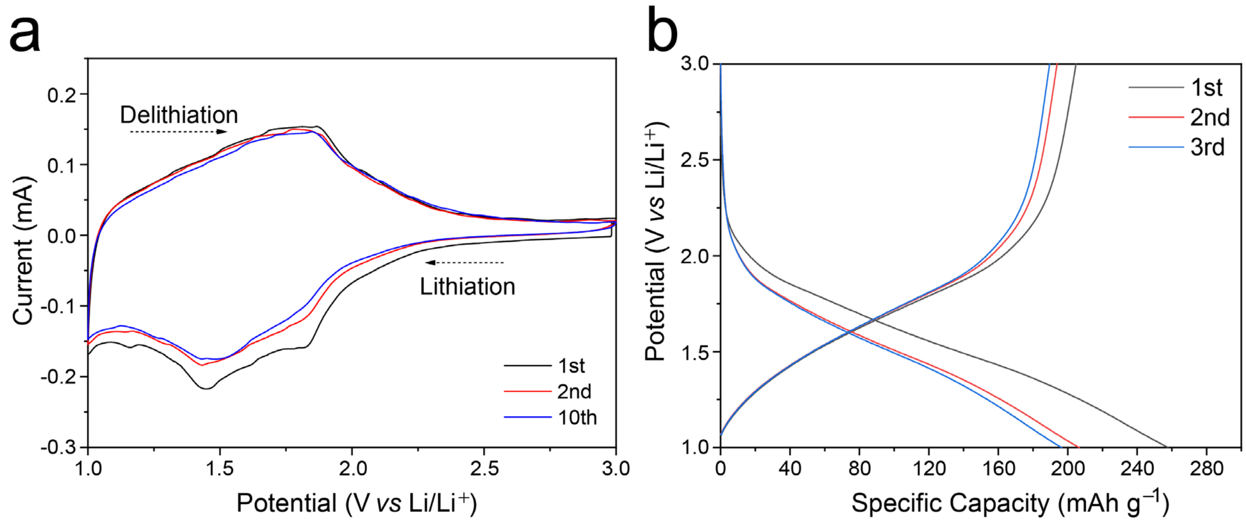

Fig. S5 Electrochemical performances of T-Nb_2O_5/C-PVDF in a half-cell with a potential window of 1.0-3.0 V. (a) CV curves for the 1st, 2nd and 10th cycles at a scan rate of 0.2 mV s^{-1}, (b) GCD curves at 0.1 A g^{-1}.

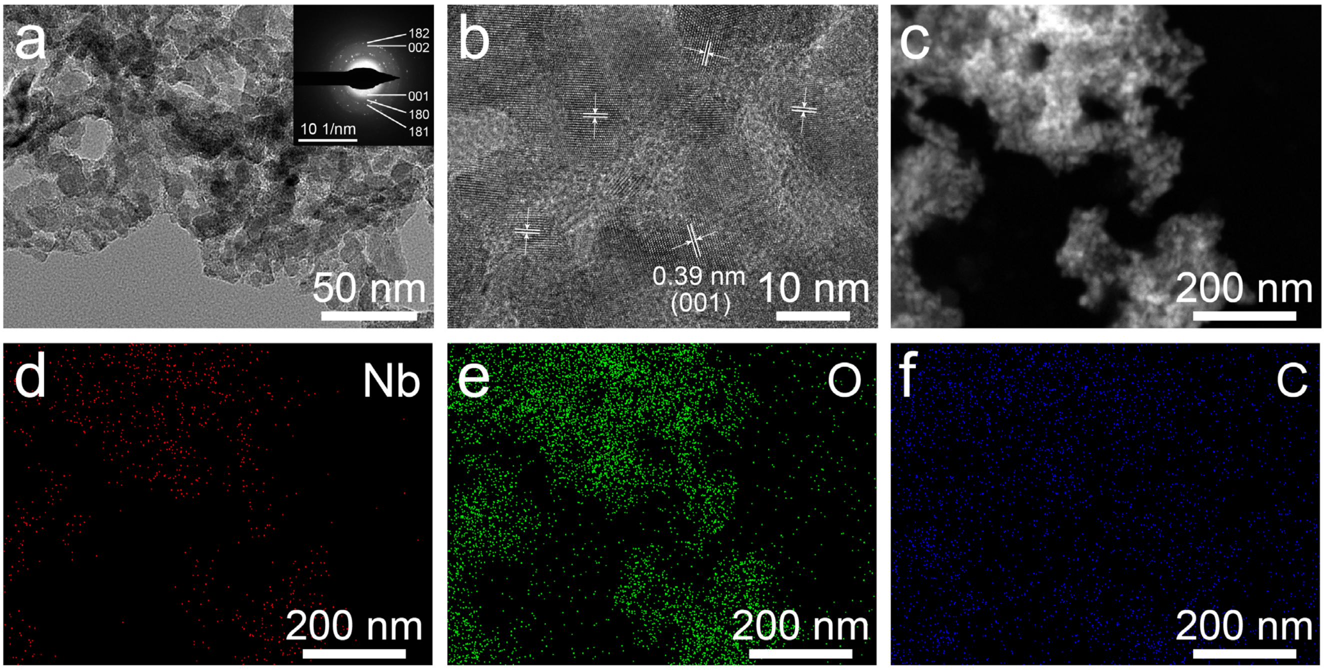

Fig. S6 TEM images of T-Nb_2O_5/C-SA anodes after 100 cycles at 0.1 A g^{-1}.

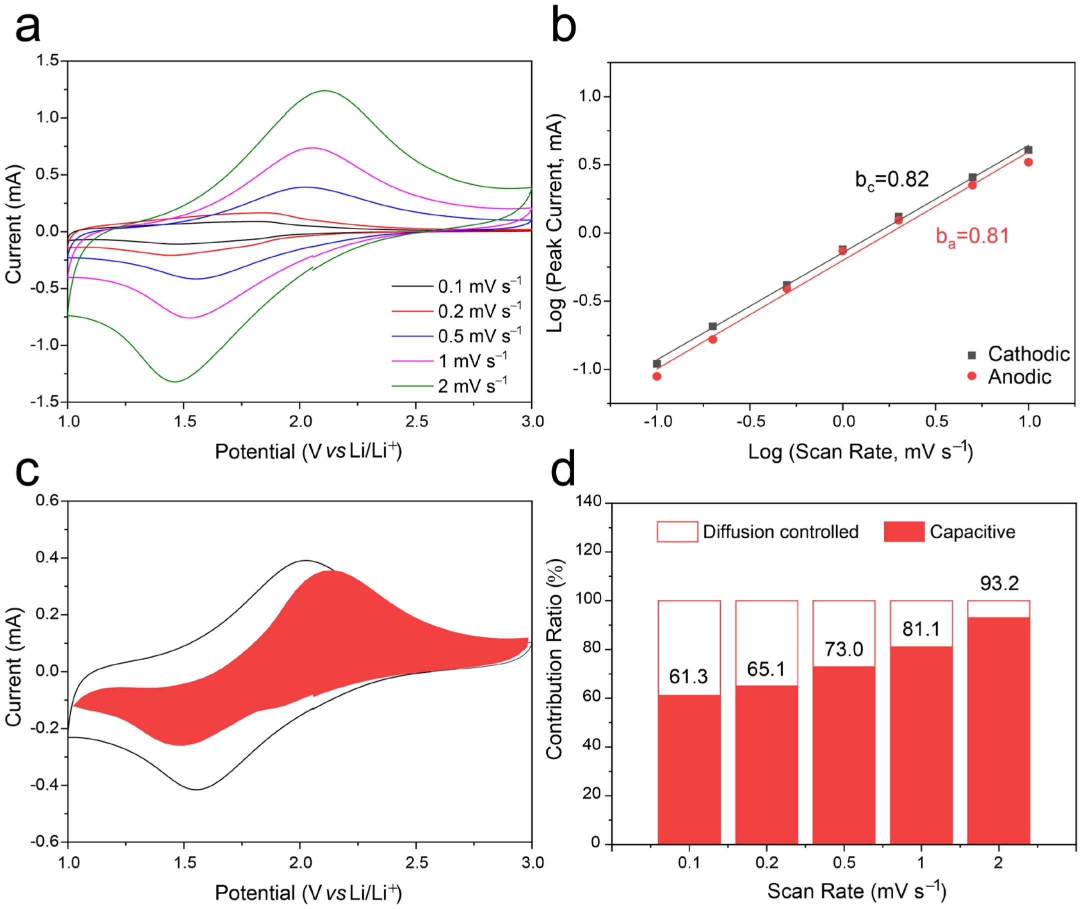

Fig. S7 (a) CV curves of T-Nb_2O_5/C-SA at various scan rates from 0.1 to 2 mV s^{-1}, (b) logarithmic relationships between the peak currents and scan rates, (c) CV curve of T-Nb_2O_5/C-SA with separation between total current (black line) and capacitive current (red region) at 0.5 mV s^{-1}, and (d) calculated contributions of capacitive capacities and diffusion-limited capacities at various scan rates.

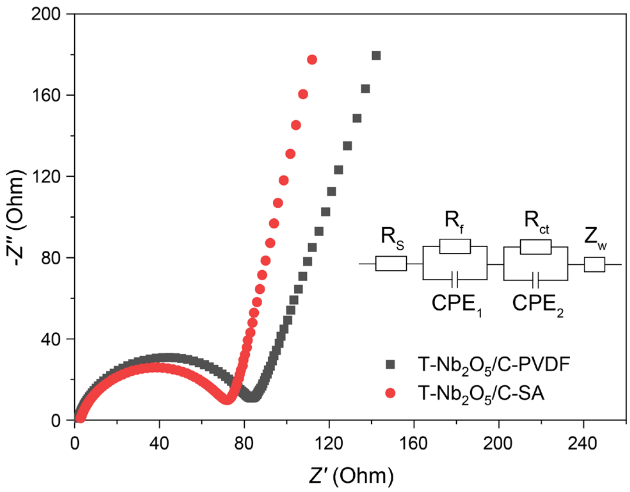

Fig. S8 Nyquist plots of T-Nb_2O_5/C based electrodes with different binders. The inset is an equivalent circuit (R_f is the migration impedance of lithium ions through the solid electrolyte interface film, Z_w is the Warburg impedance, and CPE_1 and CPE_2 are constant phase elements).

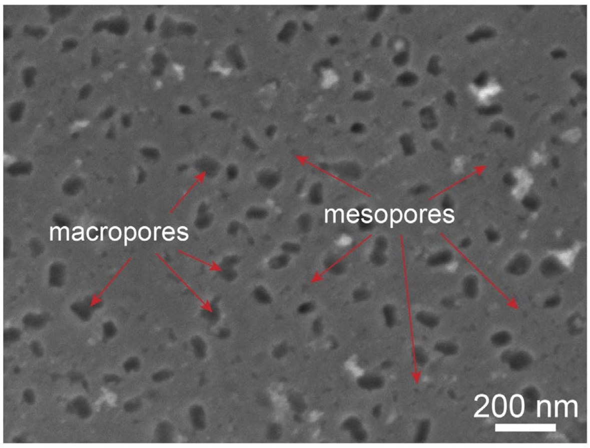

Fig. S9 SEM image at higher magnification of T-SDC.

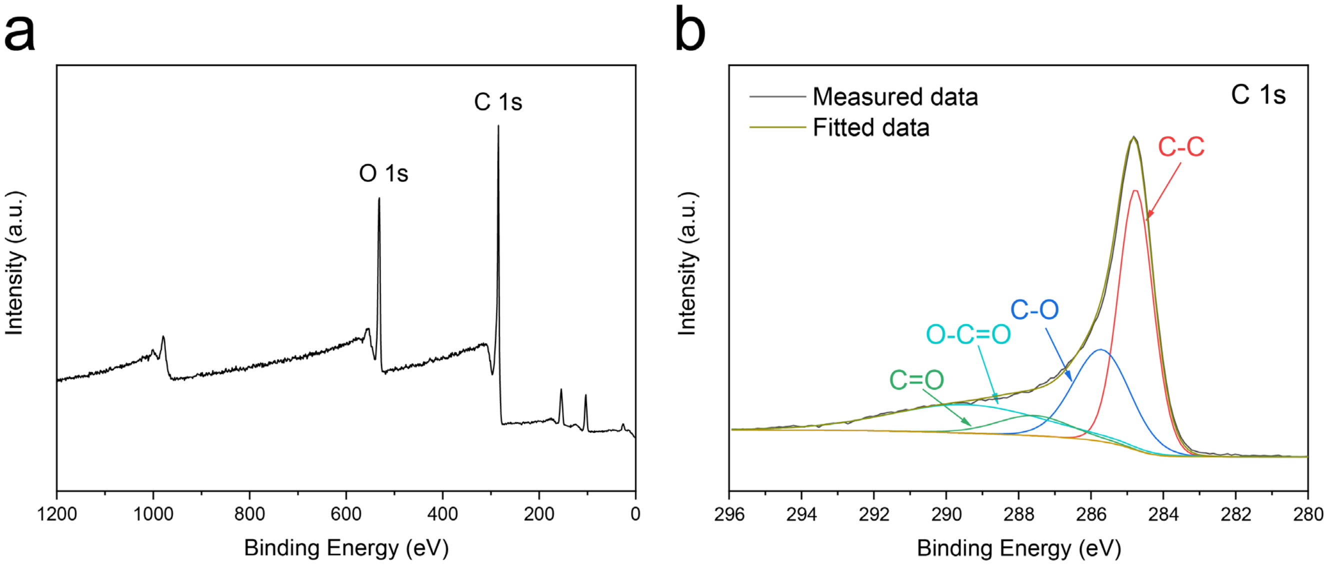

Fig. S10 XPS spectra of T-SDC: (a) full, (b) C 1s.

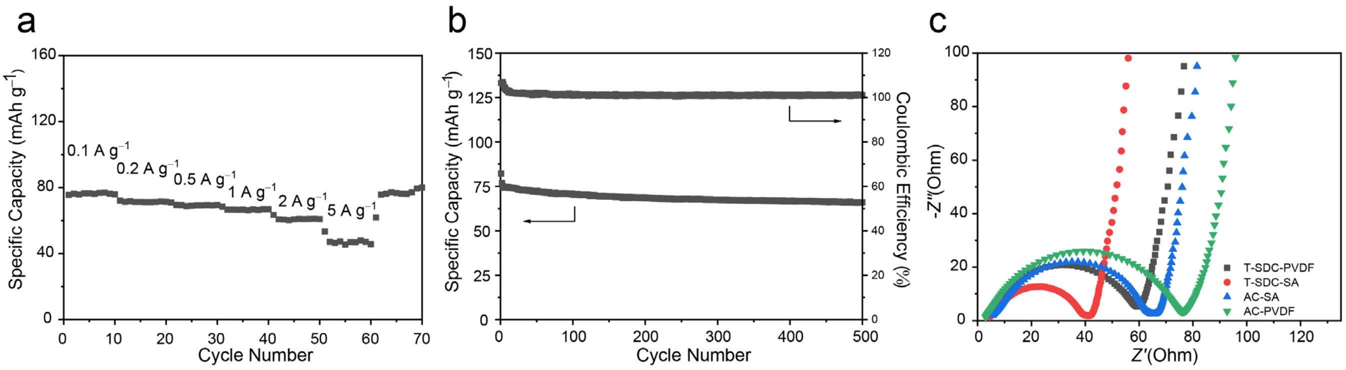

Fig. S11 (a) Rate performance and (b) cycling performance for 500 cycles at 1 A g^{-1} of the AC-PVDF electrode with a voltage window of 2.0-4.5 V, and (c) Nyquist plots of the T-SDC-SA, T-SDC-PVDF, AC-SA and AC-PVDF electrodes.

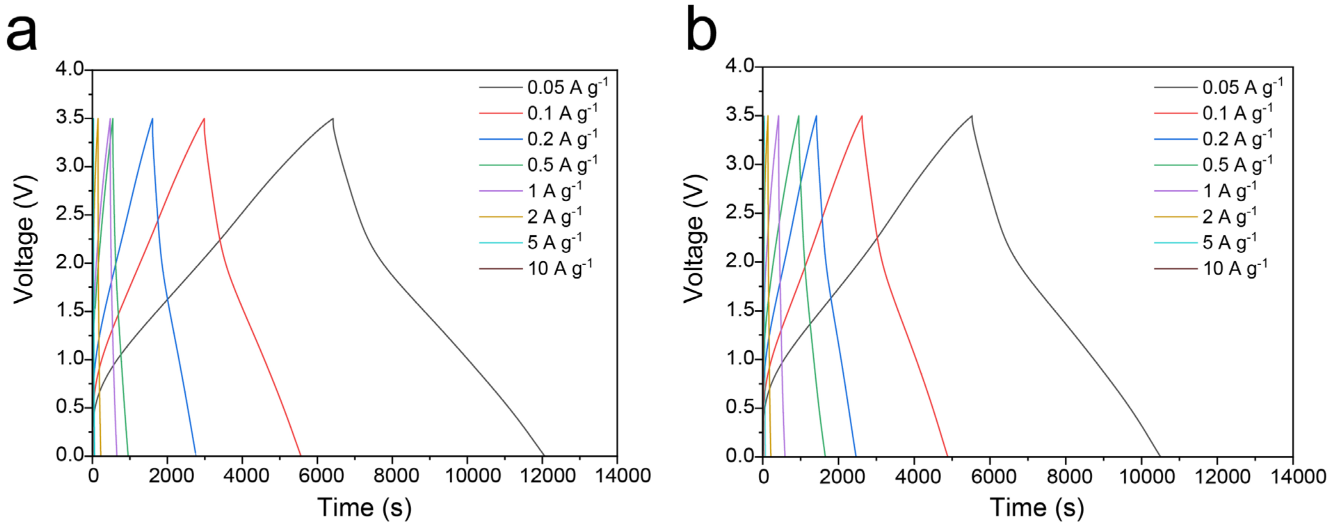

Fig. S12 GCD profiles of assembled LICs at current densities from 0.05 to 10 A g^{-1}. (a) T-Nb_2O_5/C//T-SDC-PVDF, (b) T-Nb_2O_5/C//AC.

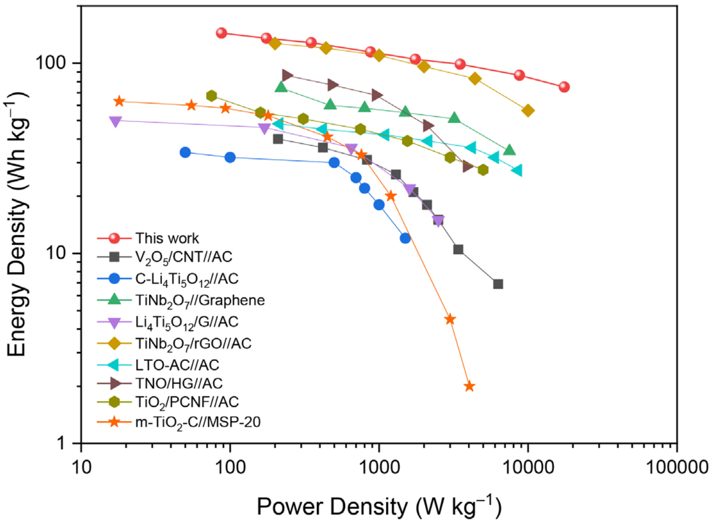

Fig. S13 Ragone plots of the all alginate-derived T-Nb_2O_5/C//T-SDC LIC compared to reported LICs based on other materials.

Table S1 Porous structure characteristics of T-Nb_2O_5/C hybrid and T-SDC.

	S_{BET} (m^2 g^{-1})	**S_{mi}** (m^2 g^{-1})	**S_{me}** (m^2 g^{-1})	**V_t** (cm^3 g^{-1})	**V_{mi}** (cm^3 g^{-1})	**V_{me}** (cm^3 g^{-1})
T-Nb_2O_5/C	161.4	51.1	110.3	0.382	0.043	0.339
T-SDC	3320.7	324.4	2996.3	2.176	0.672	1.504

S_{mi}, specific surface area of the micropores; S_{me}, specific surface area of the mesopores; V_t, total pore volume; V_{mi}, pore volume of micropores; V_{me}, pore volume of mesopores.

Table S2 Performance of different T-Nb_2O_5-based LICs.

Materials (anode//cathode)	Energy Density ($W h kg^{-1}$)	Power Density ($kW kg^{-1}$)	Cycle Performance	Ref.
T-Nb_2O_5/C//T-SDC	143.9 at 87.6 $W kg^{-1}$	17.5 at 75.1 $W h kg^{-1}$	84.6%, 3000 cycles	**This work**
Nb_2O_5/NC//NCC	67.2 at 175 $W kg^{-1}$	8.75 at 40.8 $W h kg^{-1}$	82.1%, 3000 cycles	1
T-Nb_2O_5/NC//AC	49.7	8.75	91.1%, 1000 cycles	2
T-Nb_2O_5/GA//AGF	53 at 355 $W kg^{-1}$	2 at 19.7 $W h kg^{-1}$	99%, 3000 cycles	3
3D-Nb_2O_5/C//AC	96.8	41	75%, 3000 cycles	4
Nb_2O_5/MC//MCHS	38 at 320 $W kg^{-1}$	16 at 12 $W h kg^{-1}$	87%, 3000 cycles	5
T-Nb_2O_5/CNW//ACNs	80 at 180 $W kg^{-1}$	5.3 at 24 $W h kg^{-1}$	80%, 35000 cycles	6
T-Nb_2O_5/C//NCs	63 at 70 $W kg^{-1}$	16.5 at 5 $W h kg^{-1}$	80%, 1000 cycles	7
m-Nb_2O_5/C//MSP-20	74	18.5 at 15 $W h kg^{-1}$	90%, 1000 cycles	8
T-Nb_2O_5/rGO//AC	45.1 at 715.2 $W kg^{-1}$	14.7 at 24 $W h kg^{-1}$	71.6%, 4000 cycles	9
T-Nb_2O_5/NC//AC	76.9 at 450 $W kg^{-1}$	11.25 at 22.4 $W h kg^{-1}$	85%, 4500 cycles	10
Nb_2O_5/CNT//AC	33.5 at 82 $W kg^{-1}$	4 at 4 $W h kg^{-1}$	/	11
L-Nb_2O_5/rGO//C	106 at 580 $W kg^{-1}$	14 at 32 $W h kg^{-1}$	/	12
Nb_2O_5/C//AC	43.4 at 375 $W kg^{-1}$	7.5 at 10.8 $W h kg^{-1}$	82.3%, 3000 cycles	13
T-Nb_2O_{5-x}/NC//AC	56.7	9.75	/	14
T-Nb_2O_5 NRs//AC	92.1 at 80 $W kg^{-1}$	8 at 35.6 $W h kg^{-1}$	95%, 4000 cycles	15
H-Nb_2O_5/rGO//SCCB	100.2 at 50 $W kg^{-1}$	20 at 18.3 $W h kg^{-1}$	82%, 3000 cycles	16
M-Nb_2O_5@C/rGO//AC	71.5 at 247 $W kg^{-1}$	3.9 at 18.3 $W h kg^{-1}$	94%, 2500 cycles	17

Table S3 Performance of LICs based on different electrode materials.

Materials (anode//cathode)	Energy Density ($W h kg^{-1}$)	Power Density ($kW kg^{-1}$)	Cycle Performance	Ref.
T-Nb_2O_5/C//T-SDC	143.9 at 87.6 $W kg^{-1}$	17.5 at 75.1 $W h kg^{-1}$	84.6%, 3000 cycles	**This work**
V_2O_5/CNT//AC	40 at 210 $W kg^{-1}$	6.3 at 6.9 $W h kg^{-1}$	80%, 1000 cycles	18
TiO_2-B//CNT	12.5	/	~ 90.6%, 600 cycles	19
C-$Li_4Ti_5O_{12}$//AC	~ 34 at 50 $W kg^{-1}$	~ 1.5 at 12 $W h kg^{-1}$	95%, 1000 cycles	20
$TiNb_2O_7$//Graphene	74	7.5 at 34.5 $W h kg^{-1}$	81.2%, 3000 cycles	21
$Li_4Ti_5O_{12}$/G//AC	50	2.5 at 15 $W h kg^{-1}$	75%, 1000 cycles	22
$TiNb_2O_7$/rGO//AC	127 at 200 $W kg^{-1}$	10 at 56.4 $W h kg^{-1}$	86.1%, 3000 cycles	23
LTO-AC//AC	48 at 214 $W kg^{-1}$	8.56 at 27.3 $W h kg^{-1}$	79.2%, 2000 cycles	24
TNO/HG//AC	86.3 at 237.7 $W kg^{-1}$	3.88 at 28.7 $W h kg^{-1}$	90.2%, 3000 cycles	25
TiO_2/PCNF//AC	67.4 at 75 $W kg^{-1}$	5 at 27.5 $W h kg^{-1}$	80.5%, 10000 cycles	26
m-TiO_2-C//MSP-20	63	4.044	/	27

References

1 Y. Lian; Z. Xu; D. Wang; Y. Bai; C. Ban; J. Zhao; H. Zhang, *Journal of Alloys and Compounds*, 2021, **850**, 156808.

2 Y. Lian; D. Wang; S. Hou; C. Ban; J. Zhao; H. Zhang, *Electrochimica Acta*, 2020, **330**, 135204.

3 Y. Li; R. Wang; W. Zheng; Q. Zhao; S. Sun; G. Ji; S. Li; X. Fan; C. Xu, *Materials Technology*, 2020, **35** (9-10), 625-634.

4 H. Li; D. Li; J. Shi; Z. He; Z. Zhao; H. Wang, *Sustainable Energy & Fuels*, 2020, **4** (9), 4868-4877.

5 S. Zhang; J. Wu; J. Wang; W. Qiao; D. Long; L. Ling, *Journal of Power Sources*, 2018, **396**, 88-94.

6 M. Y. Song; N. R. Kim; H. J. Yoon; S. Y. Cho; H. J. Jin; Y. S. Yun, *ACS Appl Mater Interfaces*, 2017, **9** (3), 2267-2274.

7 E. Lim; C. Jo; H. Kim; M.-H. Kim; Y. Mun; J. Chun; Y. Ye; J. Hwang; K.-S. Ha; K. C. Roh; K. Kang; S. Yoon; J. Lee, *ACS Nano*, 2015, **9** (7), 7497-7505.

8 E. Lim; H. Kim; C. Jo; J. Chun; K. Ku; S. Kim; H. I. Lee; I.-S. Nam; S. Yoon; K. Kang; J. Lee, *Acs Nano*, 2014, **8** (9), 8968-8978.

9 Y. Jiao; H. Zhang; H. Zhang; A. Liu; Y. Liu; S. Zhang, *Nano Research*, 2018, **11** (9), 4673-4685.

10 S. Liu; J. Zhou; Z. Cai; G. Fang; Y. Cai; A. Pan; S. Liang, *Journal of Materials Chemistry A*, 2016, **4** (45), 17838-17847.

11 X. Wang; G. Li; Z. Chen; V. Augustyn; X. Ma; G. Wang; B. Dunn; Y. Lu, *Advanced Energy Materials*, 2011, **1** (6), 1089-1093.

12 H. Song; J. Fu; K. Ding; C. Huang; K. Wu; X. Zhang; B. Gao; K. Huo; X. Peng; P. K. Chu, *Journal of Power Sources*, 2016, **328**, 599-606.

13 X. Wang; C. Yan; J. Yan; A. Sumboja; P. S. Lee, *Nano Energy*, 2015, **11**, 765-772.

14 Y. Lian; Y. Zheng; Y. Bai; D. Wang; H. Yan; Z. Wang; J. Zhao; H. Zhang, *Journal of Power Sources*, 2021, **507**, 230267.

15 L. Qin; Y. Liu; S. Xu; S. Wang; X. Sun; S. Zhu; L. Hou; C. Yuan, *Small Methods*, 2020, **4** (12),2000630.

16 S. Li; T. Wang; W. Zhu; J. Lian; Y. Huang; Y.-Y. Yu; J. Qiu; Y. Zhao; Y.-C. Yong; H. Li, *Journal of Materials Chemistry A*, 2019, **7** (2), 693-703.

17 X. Jiao; Q. Hao; X. Xia; Z. Wu; W. Lei, *Chemical Communications*, 2019, **55** (18), 2692-2695.

18 Z. Chen; V. Augustyn; J. Wen; Y. Zhang; M. Shen; B. Dunn; Y. Lu, *Adv Mater*, 2011, **23** (6), 791-795.

19 Q. Wang; Z. H. Wen; J. H. Li, *Advanced Functional Materials*, 2006, **16** (16), 2141-2146.

20 H.-G. Jung; N. Venugopal; B. Scrosati; Y.-K. Sun, *Journal of Power Sources*, 2013, **221**, 266-271.

21 H. Li; L. Shen; J. Wang; S. Fang; Y. Zhang; H. Dou; X. Zhang, *Journal of Materials Chemistry A*, 2015, **3** (32), 16785-16790.

22 H. Kim; K.-Y. Park; M.-Y. Cho; M.-H. Kim; J. Hong; S.-K. Jung; K. C. Roh; K. Kang, *ChemElectroChem*, 2014, **1** (1), 125-130.

23 Y. Li; Y. Wang; R. Cai; C. Yu; J. Zhang; J. Wu; C. S. Tiwary; J. Cui; Y. Zhang; Y. Wu, *J Colloid Interface Sci*, 2022, **610**, 385-394.

24 C. Jiang; J. Zhao; H. Wu; Z. Zou; R. Huang, *Journal of Power Sources*, 2018, **401**, 135-141.

25 X. Jiao; Q. Hao; X. Xia; D. Yao; Y. Ouyang; W. Lei, *Journal of Power Sources*, 2018, **403**, 66-75.

26 C. Yang; J. L. Lan; W. X. Liu; Y. Liu; Y. H. Yu; X. P. Yang, *ACS Appl Mater Interfaces*, 2017, **9** (22), 18710-18719.

27 Y. Lee; S. Kim; J. H. Lee; K. C. Roh; E. Lim; J. Lee, *RSC Advances*, 2019, **9** (65), 37882-37888.